Pairing Effects on the Fragment Mass Distribution of Th, U, Pu, and Cm Isotopes[*]

Xin Guan,[1,†] Jin-Huan Zheng,[1] and Mei-Yan Zheng[1]

[1]*Department of Physics, Liaoning Normal University, Dalian 116029, China*

This article presents a comprehensive study on the fission process in Th, U, Pu, and Cm isotopes using a Yukawa-folded mean-field plus standard pairing model. The focus is on analyzing the effects of the pairing interaction on the fragment mass distribution and its dependence on nuclear elongation. The study demonstrates that the pairing interaction plays an important role in the fragment mass distribution for ^{230}Th, ^{234}U, ^{240}Pu, and ^{246}Cm. Numerical analysis reveals that increasing the pairing interaction strength leads to a decrease in asymmetric fragment mass distribution and an increase in symmetric distribution. Furthermore, the investigation examines the odd-even mass differences at symmetric and asymmetric fission points, highlighting their sensitivity to changes in the pairing interaction strength. The systematic analysis of Th, U, Pu, and Cm isotopes' fragment mass distributions demonstrates the effectiveness of the model in reproducing experimental data. Additionally, the study explores the effects of the zero-point energy parameter and neck-breaking probability parameter on the fragment mass distribution for ^{240}Pu. In conclusion, this research provides valuable insights into the fission process by emphasizing the importance of the pairing interaction and its relationship with nuclear elongation.

Keywords: Nuclear fission; Pairing interaction; Fragment Mass Distribution; Actinide nuclei

I. INTRODUCTION

Nuclear fission is a fundamental process that plays a central role in modern nuclear technology. The theoretical calculation of the fission process is a complex and challenging problem, necessitating the utilization of advanced nuclear models and computational techniques [1–6]. Throughout the years, numerous theoretical models have been developed to predict fission yields, ranging from simple empirical models to sophisticated microscopic models based on nuclear structure and reaction theory [7–9]. These models have been validated against experimental data and proven to be valuable tools for predicting the behavior of nuclear systems.

Pairing interactions have a significant impact on the properties of the fissioning nucleus and the resulting fission products. For instance, the strength of the pairing interaction strongly influences the shape of the barriers separating the ground state from scission [10–21] fission fragment distributions [22–25], and spontaneous fission lifetimes [26]. In the dynamical description of nuclear fission, pairing interaction should be considered on the same footing as those associated with shape degrees of freedom [15]. Understanding the role of pairing interactions in nuclear fission is an active area of research, and various theoretical models have been developed to describe their behavior in different fission scenarios. Macroscopic-microscopic studies have demonstrated that pairing fluctuations can significantly reduce collective action and affect the predicted spontaneous fission lifetimes [27]. In the Hartree-Fock-Bogoliubov (HFB) model, pairing can be self-consistently included by extending the trial space to quasi-particle Slater determinants [22, 28]. Theoretical works based on the HFB method have revealed that the effect of pairing interactions hinders collective rotation, reduces level crossings, and thus shortens the half-lives of spontaneous fission [29]. The role of dynamical pairing in induced fission dynamics has been investigated using the time-dependent generator coordinate method in the Gaussian overlap approximation, based on the microscopic framework of nuclear energy density functionals [30]. It has been shown that the inclusion of dynamical pairing has a pronounced effect on collective inertia, the collective flux through the scission hypersurface, and the resulting fission yields. The latest research on the fission dynamics mechanism of ^{240}Pu, based on the time-dependent Hartree-Fock method, demonstrates that as dynamical pairing diminishes at high excitations, the random transition between single-particle levels around the Fermi surface, to mimic thermal fluctuations, becomes indispensable in driving fission [31].

In recent studies, an iterative algorithm [32, 33] has been employed to investigate the fission barriers and static fission paths of Th, U, and Pu isotopes using the deformed mean-field plus standard pairing model with an exact pairing solution [34]. This innovative approach provides a precise representation of pairing interactions in nuclear fission, avoiding artifacts introduced by BCS calculations, such as non-conservation of particle numbers and pairing collapse phenomena [11]. The comprehensive investigation of the inner and outer fission barriers in even-even nuclei Th, U, and Pu isotopes clearly demonstrates the standard pairing model's ability to closely replicate the experimental inner and outer barrier heights in comparison to the BCS scheme [34]. Moreover, employing the deformed mean-field plus standard pairing model, researchers have explored the influence of pairing interactions on scission configurations, total kinetic energy, and mass distributions of U isotopes [35]. The model successfully reproduces the total kinetic energy and fragment mass distributions of $^{232-238}$U isotopes, exhibiting excellent agreement with experimental data. The results highlight the scission region's sensitivity to variations in pairing interaction strength, particularly for asymmetric and symmetric scis-

* Supported by the National Natural Science Foundation of China (No.12275115,12175097) and the educational department of Liaoning province (No. LJKMZ20221410).

† Corresponding author, Xin Guan, guanxin@lnnu.edu.cn.

sion points. Notably, changes in the peak-to-valley ratio of the mass distribution, resulting from variations in the pairing interaction strength, underscore the significant impact of pairing interactions on the fission process of ^{236}U within this model.

It is crucial to develop a reliable and valid model to characterize the fragment mass distribution, and actinide nuclei serve as important regions to test the reliability of these models. Therefore, extending our previous work to describe actinide nuclei and studying the influence of interactions on the fragment mass distribution is both necessary and meaningful.

This investigation presents a systematic analysis of fission fragment mass distributions in Th, U, Pu, and Cm isotopes using the deformed mean-field plus standard pairing model. The potential energy is calculated within the macroscopic-microscopic framework, incorporating the Fourier shape parametrization combined with the LSD model + Yukawa-folded potential. The mass distribution of fission fragments is described using the three-dimensional collective model of the Born-Oppenheimer approximation (BOA). Building upon our previous work in Ref. [35], this study offers a comprehensive analysis of the pairing's impact on the mass distribution of fission fragments across the Th, U, Pu, and Cm isotopes chain.

II. THEORETICAL FRAMEWORK AND NUMERICAL DETAILS

A. Deformed mean-field plus standard pairing model

The Hamiltonian of the deformed mean-field plus standard pairing model for either the proton or the neutron sector is given by

$$\hat{H} = \sum_{i=1}^{n} \varepsilon_i \hat{n}_i - G \sum_{ii'} S_i^+ S_{i'}^- . \tag{1}$$

Here, the sums run over all given i-double degeneracy levels of total number n, $G > 0$ represents the overall pairing interaction strength. The single-particle energies εi are obtained from mean-field methods, such as Yukawa-folded single-particle potential, Woods-Saxon potential (WS), Hartree-Fock (HF). The fermion number operator for the i-th double degeneracy level is defined as $n_i = a_{i\uparrow}^\dagger a_{i\uparrow} + a_{i\downarrow}^\dagger a_{i\downarrow}$, and the pair creation (annihilation) operator is represented by $S_i^+ = a_{i\uparrow}^\dagger a_{i\downarrow}^\dagger$ $[S_i^- = (S_i^+)^\dagger = a_{i\downarrow} a_{i\uparrow}]$. The up and down arrows in these expressions refer to time-reversed states.

Using the Richardson-Gaudin method [36–41], the exact k-pair eigenstates of (1) with $\nu_{i'} = 0$ for even systems or $\nu_{i'} = 1$ for odd systems, where i' is the label of the double degeneracy level occupied by an unpaired single particle, can be expressed as:

$$|k; \xi; \nu_{i'}\rangle = S^+(x_1^{(\xi)}) S^+(x_2^{(\xi)}) \cdots S^+(x_k^{(\xi)}) |\nu_{i'}\rangle, \tag{2}$$

where $|\nu_{i'}\rangle$ is the pairing vacuum state with the seniority $\nu_{i'}$ that satisfies $S_i^- |\nu_{i'}\rangle = 0$ and $\hat{n}_i |\nu_{i'}\rangle = \delta_{ii'} \nu_i |\nu_{i'}\rangle$ for all i.

Here, ξ is an additional quantum number for distinguishing different eigenvectors with the same quantum number k and

$$S^+(x_\mu^{(\xi)}) = \sum_{i=1}^{n} \frac{1}{x_\mu^{(\xi)} - 2\varepsilon_i} S_i^+, \tag{3}$$

in which the spectral parameters $x_\mu^{(\xi)}$ $(\mu = 1, 2, \ldots, k)$ satisfy the following set of Bethe ansatz equations (BAEs):

$$1 + G \sum_i \frac{\Omega_i}{x_\mu^{(\xi)} - 2\varepsilon_i} - 2G \sum_{\mu'=1(\neq\mu)}^{k} \frac{1}{x_\mu^{(\xi)} - x_{\mu'}^{(\xi)}} = 0, \tag{4}$$

where the first sum runs over all i levels and $\Omega_i = 1 - \delta_{ii'} \nu_{i'}$. For each solution, the corresponding eigenenergy is given by

$$E_k^{(\xi)} = \sum_{\mu=1}^{k} x_\mu^{(\xi)} + \nu_{i'} \varepsilon_{i'} . \tag{5}$$

The general method to find solutions of Eq.(4) is based on the polynomial approach described in Refs.[42–45]. This approach involves solving the second-order Fuchsian equation [46], given by:

$$A(x)P''(x) + B(x)P'(x) - V(x)P(x) = 0, \tag{6}$$

where $A(x) = \prod_{i=1}^{n} (x_\mu^{(\xi)} - 2\varepsilon_i)$ is an n-degree polynomial,

$$B(x)/A(x) = -\sum_{i=1}^{n} \frac{\Omega_i}{x_\mu^{(\xi)} - 2\varepsilon_i} - \frac{1}{G}. \tag{7}$$

The polynomials $V(x)$, also known as Van Vleck polynomials [46], are of degree $n - 1$ and are determined based on Eq. (6). They are defined as follows:

$$V(x) = \sum_{i=0}^{n-1} b_i x^i. \tag{8}$$

The polynomials $P(x)$ with zeros corresponding to the solutions of Eq. (4) is defined as

$$P(x) = \prod_{i=1}^{k} (x - x_i^{(\xi)}) = \sum_{i=0}^{k} a_i x^i. \tag{9}$$

Here, k represents the number of pairs, and b_i and a_i are the expansion coefficients that need to be determined instead of the Richardson variables x_i. Additionally, when we set $a_k = 1$ in $P(x)$, the coefficient a_{k-1} is equal to the negative sum of the $P(x)$ zeros, i.e., $a_{k-1} = -\sum_{i=1}^{k} x_i^{(\xi)} = -E_k^{(\xi)}$.

For doubly degenerate systems with $\Omega_i = 1$, if the value of x approaches twice the single-particle energy of a given level δ, i.e., $x = 2\varepsilon_\delta$, we can rewrite Eq.(6) as follows[42, 45]:

$$\left(\frac{P'(2\varepsilon_\delta)}{P(2\varepsilon_\delta)}\right)^2 - \frac{1}{G}\left(\frac{P'(2\varepsilon_\delta)}{P(2\varepsilon_\delta)}\right) = \sum_{i\neq\delta} \frac{\left[\left(\frac{P'(2\varepsilon_\delta)}{P(2\varepsilon_\delta)}\right) - \left(\frac{P'(2\varepsilon_i)}{P(2\varepsilon_i)}\right)\right]}{2\varepsilon_\delta - 2\varepsilon_i} \tag{10}$$

The iterative algorithm for obtaining the exact solution of the standard pairing problem using the Richardson-Gaudin method is established, employing the polynomial approach described in Eq.(10)[32]. This algorithm showcases remarkable efficiency and robustness, capable of handling both spherical and deformed systems on a large scale. A crucial element contributing to its success lies in the determination of initial guesses for the large-set nonlinear equations, ensuring control and adherence to fundamental physical principles. Moreover, the algorithm effectively tackles the challenges of nonsolutions and numerical instabilities frequently encountered in existing approaches by reducing the high-dimensional problem to a one-dimensional Monte Carlo sampling procedure. Leveraging this innovative iterative algorithm, we employed the model to explore actinide nuclei isotopes, resulting in exceptional agreement with experimental data [32–35].

B. The Fourier shape parametrization

Recent studies have highlighted the remarkable efficiency of the Fourier parametrization when describing the essential features of deformed nuclear shapes, extending up to the scission configuration [7, 47]. Building upon these findings, the present work employs the innovative Fourier parametrization of nuclear shapes in conjunction with the LSD + Yukawa-folded macroscopic-microscopic potential-energy prescription, yielding highly efficient results [35, 48, 49]. Specifically, the macroscopic-microscopic framework introduced in Ref. [35] serves as the primary foundation for this study. In this framework, the single-particle energies ε_i in the model Hamiltonian (1) are derived from the Yukawa-folded potential. The expansion of the nuclear surface, expressed as a Fourier series in terms of dimensionless coordinates, is given by:

$$\begin{aligned}\frac{\rho_s^2(z)}{R_0^2} = \sum_{n=1}^{\infty}\Big[a_{2n}\cos\Big(\frac{(2n-1)\pi}{2}\frac{z-z_{\rm sh}}{z_0}\Big)\\ +a_{2n+1}\sin\Big(\frac{2n\pi}{2}\frac{z-z_{\rm sh}}{z_0}\Big)\Big],\end{aligned} \tag{11}$$

where $\rho^2 s(z)$ represents the distance from a surface point to the symmetry z-axis, and $R0 = 1.2A^{1/3}$ fm corresponds to the radius of the corresponding spherical shape with the same volume. The shape extends along the symmetry axis by $2z_0$, with the left and right ends located at $z_{\rm min} = z_{\rm sh} - z_0$ and $z_{\rm max} = z_{\rm sh}+z_0$, respectively. Here, z_0 is half of the extension of the shape along the symmetry axis, derived from volume conservation, and $z_{\rm sh}$ is determined to ensure the center of mass of the nuclear shape is positioned at the origin of the coordinate system. Following the convergence properties discussed in Ref. [7], we retain the first five orders $a_2, \ldots, a_6$ as a starting point, and transform the parameters a_n into the deformation parameters q_n as follows:

$$\begin{aligned}q_2 &= a_2^{(0)}/a_2 - a_2/a_2^{(0)},\\ q_3 &= a_3,\\ q_4 &= a_4 + \sqrt{(q_2/9)^2 + (a_4^{(0)})^2},\\ q_5 &= a_5 - (q_2-2)a_3/10,\\ q_6 &= a_6 - \sqrt{(q_2/100)^2 + (a_6^{(0)})^2},\end{aligned} \tag{12}$$

where $a_n^{(0)}$ representing the values of the Fourier coefficients for the spherical shape. While the higher-order coordinates q_5 and q_6 are typically negligible within the current approach's accuracy, the set of q_i possesses explicit physical significance in characterizing the nuclear fission process. Specifically, q_2 denotes the elongation of the nucleus, q_4 represents the neck parameter, and q_3 reflects the left-right asymmetry parameter. For this study, the dynamic process of nuclear fission will be modeled in the three-dimensional deformation space $(q_2, q_3; q_4)$ using the Fourier shape parametrization. It is important to note that the present work does not consider nonaxially symmetric shapes since they primarily play a significant role in the vicinity of the ground state and the first saddle point.

C. The mass distributions

In previous studies, the use of Wigner functions to approximate the probability distribution associated with neck and mass asymmetry degrees of freedom has shown good agreement between model predictions and experimental results [7, 49–52]. Building on these ideas, this study proposes a fission dynamics scenario where the motion towards fission primarily occurs along the q_2 direction, accompanied by fast vibrations in the perpendicular q_3 and q_4 collective variables. The total eigenfunction $\psi_{nE}(q_2, q_3, q_4)$ of the fissioning nucleus is then approximated as the product of two functions:

$$\psi_{nE}(q_2,q_3,q_4) = \mu_{nE}(q_2)\phi_n(q_3,q_4;q_2). \tag{13}$$

$\mu_{nE}(q_2)$, which depends mainly on a single variable q_2 and describes the motion towards fission, and $\phi_n(q_3, q_4; q_2)$, which simulates n-phonon fast collective vibrations on the perpendicular 2D plane q_3, q_4 for a given elongation q_2. For low-energy fission, only the lowest energy eigenstate $\phi_{n=0}$ is considered.

The density of probability $W(q_3, q_4; q_2)$ of finding the system for a given elongation q_2 ,within the area of $(q_3 \pm dq_3, q_4 \pm dq_4)$, is given as

$$W(q_3,q_4;q_2) = |\psi(q_2,q_3,q_4)|^2 = |\phi_0(q_3,q_4;q_2)|^2. \tag{14}$$

To take into account the fission process, a Wigner function is employed, which is given by:

$$W(q_3,q_4;q_2) \propto \exp\Big\{-\frac{\mathrm{V(q_3,q_4;q_2)-V_{min}(q_2)}}{\mathrm{E_0}}\Big\}. \tag{15}$$

where $V_{\min}(q_2)$ is the minimum potential for a given elongation q_2, and E_0 is the zero-point energy, treated as an adjustable parameter.

To obtain the fragment mass yield for a given elongation q_2, the probabilities coming from different neck shapes, simulated by the q_4 parameter, are integrated as

$$w(q_3;q_2) = \int W(q_3,q_4;q_2)dq_4. \tag{16}$$

Following the concept introduced in Ref. [51], the neck rupture probability P is assumed to be equal to

$$P(q_3,q_4,q_2) = \frac{k_0}{k} P_{\text{neck}}(R_{\text{neck}}), \tag{17}$$

where k represents the momentum in the direction towards fission, and the constant parameter k_0 serves as a scaling parameter. R_{neck} is the deformation-dependent neck radius, and P_{neck} is a geometrical factor indicating the probability of neck rupture, which is proportional to the neck thickness. The expression for the geometrical probability factor $P_{\text{neck}}(R_{\text{neck}})$ can be chosen arbitrarily to some extent, such as using Fermi, Lorentz, or Gaussian functions [52]. In this study, we adopt the Gaussian form as follows:

$$P_{\text{neck}}(R_{\text{neck}}) = \exp[-\ln 2(\mathrm{R_{neck}/d})^2], \tag{18}$$

where d represents the half-width of the probability distribution, and it is treated as another adjustable parameter in this analysis. The momentum k in Eq. (17) simulates the dynamics of the fission process, which, as usual, depends on both the local collective kinetic energy $E - V(q_2)$ and the inertia towards the leading variable q_2.

$$\frac{\hbar^2 k^2}{2\overline{M}(q_2)} = E_{\text{kin}} = E - Q - V(q_2), \tag{19}$$

where $\overline{M}(q_2)$ represents the averaged inertia over the degrees of freedom q_3 and q_4 at a given elongation q_2, while $V(q_2)$ denotes the averaged potential. Here, it is assumed that the portion of the total energy converted into heat, denoted as Q, is negligibly small. A convenient approximation for the inertia $\overline{M}(q_2)$ is to employ the irrotational flow mass parameter B_{irr} [53], which is initially expressed as a function of the single collective parameter R_{12}, representing the distance between fragments, and the reduced mass μ of both fragments.

$$\overline{M}(q_2) = \mu[1 + 11.5(B_{\text{irr}}/\mu - 1)]\left(\frac{\partial R_{12}}{\partial q_2}\right)^2. \tag{20}$$

To incorporate the neck rupture probability $P(q_3,q_4;q_2)$ in Eq.(17), the integral over the probability distribution in Eq.(15) with respect to q_4 needs to be reformulated. This is achieved by expressing it as follows:

$$w(q_3;q_2) = \int W(q_3,q_4;q_2)P(q_2,q_3,q_4)dq_4. \tag{21}$$

The aforementioned approximation implies a crucial observation: for a fixed q_3 value, fission may occur within a specific range of q_2 deformations, each associated with different probabilities. To obtain the accurate fission probability distribution $w'(q_3;q_2)$ at a particular q_2 value, it is necessary to exclude fission events that occurred in previous configurations with $q_2' < q_2$. This can be achieved by applying the following expression:

$$w'(q_3;q_2) = w(q_3;q_2)\frac{1 - \int_{q_2'<q_2} w(q_3;q_2')dq_2'}{\int w(q_3;q_2')dq_2'}. \tag{22}$$

The normalized mass yield is then obtained as the sum of partial yields at different given q_2:

$$Y(q_3) = \frac{\int w'(q_3;q_2)dq_2}{\int w'(q_3;q_2)dq_3 dq_2}. \tag{23}$$

Since the scaling parameter k_0 introduced in Eq. (17) does not longer appear in the definition of the mass yield, the only free parameters, the zero-point energy parameter E_0 in Eq. (14) and the half-width parameter d appear in the probability of neck rupture (18). The free parameters in the model are the zero-point energy parameter E_0 and the half-width parameter d, with $d = 0.16R_0$ and $E_0 = 2.2$ MeV used in this work, based on their successful reproduction of experimental fragment mass yields in low-energy fission of Pt to Ra isotopes [49].

III. THE POTENTIAL ENERGY

In this study, the potential energy of the system is computed using the macroscopic-microscopic approach. The total energy of a nucleus with a specific deformation, represented as $E_{\text{total}}(N,Z,q_n)$, is determined through the following procedure:

$$E_{\text{total}}(N,Z,q_n) = E_{\text{LD}}(N,Z) + E_{\text{B}}(N,Z,q_n). \tag{24}$$

In the calculation, the total energy $E_{\text{total}}(N,Z,q_n)$ is composed of two main contributions. The first term, denoted as $E_{\text{LD}}(N,Z)$, corresponds to the macroscopic energy calculated using the standard liquid drop model. This term takes into account the proton number Z and neutron number N [54]. The second term, $E_{\text{B}}(N,Z,q_n)$, is related to the shape parameters q_2,q_3,q_4 and represents the potential-energy surface. In the current calculation, the focus is solely on this energy term, neglecting other contributions to the total energy.

$$\begin{aligned} E_{\text{B}}(N,Z,q_n) = E_{\text{def}}(N,Z,q_n) + E_{\text{shell}}(N,Z,q_n). \\ + E_{\text{pair}}(N,Z,q_n) \end{aligned} \tag{25}$$

The deformation correction energy $E_{\text{def}}(N,Z,q_2,q_3,q_4)$ is obtained from tables in Ref. [55]. The microscopic terms consist of the shell correction energy $E^{\nu(\pi)}_{\text{shell}}(N,Z,\{\varepsilon_i\},q_2,q_3,q_4)$ proposed by Strutinsky [56, 57] and the pairing interaction energy $E^{\nu(\pi)}_{\text{pair}}(N,Z,\{\varepsilon_i\},q_2,q_3,q_4)$ calculated using Eq. (1), where ν (π) represents the label of the neutron (proton) sector. The microscopic calculations involve considering 18 deformed harmonic oscillator shells in the Yukawa-folded

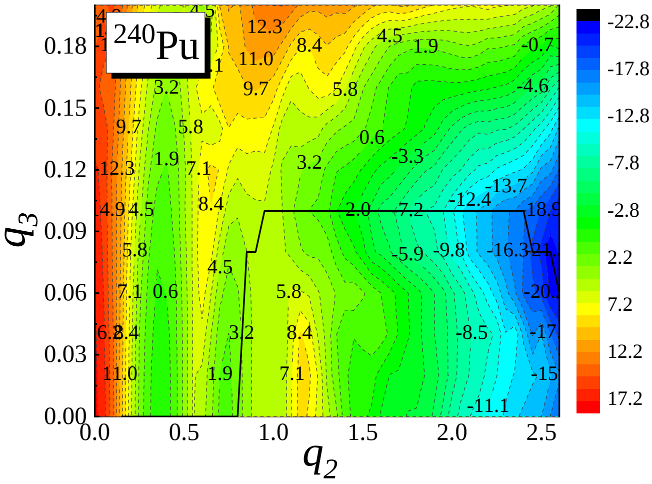

Fig. 1. (Color online) Contour map of the potential-energy surface of the nucleus ^{240}Pu (in MeV), minimized q_4 with the pairing interaction strength $G^{\nu} = 0.08$ and $G^{\pi} = 0.10$ (in MeV). The black trajectory shows the static fission path.

Table 1. Pairing interaction strength G^{ν} (G^{π}) (in MeV) for Th, U, Pu, and Cm isotopes.

	Th	U	Pu	Cm
G^{ν}	0.096	0.080	0.080	0.096
G^{π}	0.120	0.100	0.100	0.120

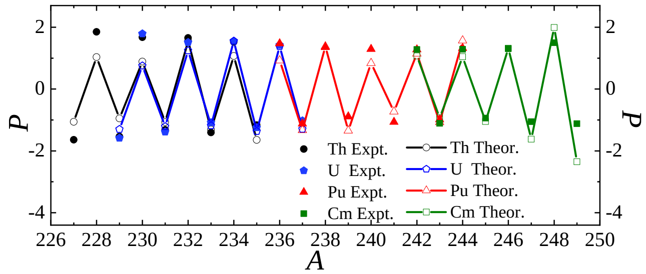

Fig. 2. (Color online) Odd-even mass differences (in MeV) for Th, U, Pu, and Cm isotopes. Experimental values are denoted as "Expt." and the theoretical values calculated in the present model are denoted as "Theor.". Experimental data are taken from Ref. [66] (in MeV).

single-particle potential to determine the single-particle energy levels. Additionally, for the pairing correction energy, 66 single-particle levels around the neutron Fermi level and 51 single-particle levels around the proton Fermi level are taken into account. To determine the overall potential-energy surface, a multidimensional minimization process is performed, simultaneously considering all axial degrees of freedom. This includes minimizing the elongation of the nucleus q_2, the asymmetry of the left and right mass fragments q_3, and the size of the neck q_4. By considering all these degrees of freedom together, a comprehensive understanding of the nuclear shape and energy landscape can be obtained.

Figure 1 illustrates the behavior of the potential-energy surface (PES) during the fission process for ^{240}Pu. At the initial stage of fission $q_2 < 0.5$, the the PES exhibits a very soft octupole deformation, and the minimum of the PES (ground-state) is located at $q_3 = 0$. The fission barrier heights obtained from the present model are in good agreement with the corresponding experimental results from Ref. [58]. Specifically, the inner barrier height is 4.88 MeV, the outer barrier height is 5.24 MeV, while the experimental results are 5.80 MeV and 5.30 MeV, respectively. Furthermore, in the asymmetric fission path, Figure 1 shows a plateau at high deformation followed by a cliff (the asymmetric scission point: $q_2 = 2.45, q_3 = 0.10, q_4 = -0.09$).

The strength of the pairing interaction G is typically determined using empirical formulas or by fitting experimental data, such as the odd-even mass difference [59–62]. Previous studies have demonstrated that pairing plays a crucial role in the region of the inner and outer barriers, and that the first and second saddle points are highly sensitive to the strength of the pairing interaction [34, 64, 65]. Therefore, in the present model, experimental observables such as the odd-even mass difference (reflecting ground-state properties) and barrier heights (reflecting excited-state properties) are used to determine the experimental values of the pairing interaction strength in the fission process.

In this paper, realistic values of the pairing interaction strengths for the isotopic chains of Th, U, Pu, and Cm were obtained by fitting the experimental values of the odd-even mass difference and the heights of the inner and outer barriers. The odd-even mass difference is calculated using the three-point formula:

$$P(A) = E_{\text{total}}(N+1, Z) + E_{\text{total}}(N-1, Z) - 2E_{\text{total}}(N, Z). \quad (26)$$

The odd-even mass difference is attributed to the presence of nucleonic pairing interactions and is highly sensitive to changes in the pairing interaction strength G [66]. The corresponding values of G^{ν} (G^{π}) are shown in Table 1.

Figure 2 clearly demonstrates that the odd-even mass differences obtained using the present approach closely match the experimental data for Th, U, Pu, and Cm isotopes. Additionally, as depicted in Fig. 3, the inner fission barriers (a) for Th, U, Pu, and Cm isotopes, as well as the outer fission barriers (b) for the same isotopes, calculated in the current model exhibit remarkable agreement with the corresponding experimental values. It is necessary to indicate that the theoretical inner barrier heights of light Th isotopes in Fig. 3-(a) are systematically lower than the experimental data, which is also reported in other calculations for light actinides in Refs. [12, 13, 67–69]. Based on analysis of different effects of neutron and proton pairing interaction on the inner and outer barrier heights in Ref. [32], the result above may be related to the strong neutron pairing interaction strength. In this article, the pairing interaction strength value in Table 1 is set to G_0^{ν} (G_0^{π}) for Th, U, Pu, and Cm isotopes.

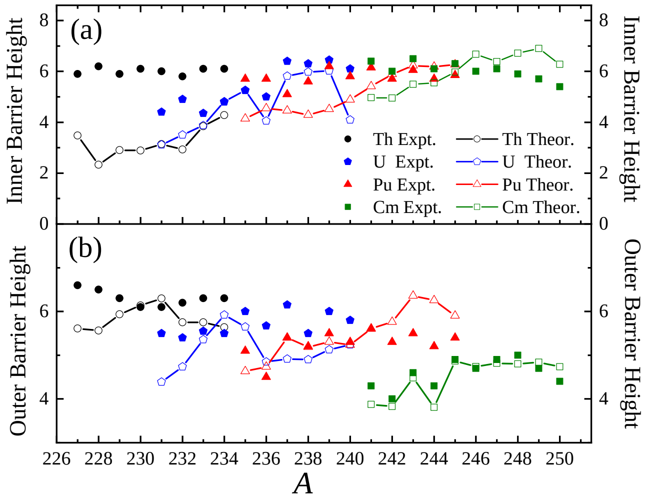

Fig. 3. (Color online) Inner fission barriers (a) and outer fission barriers (b) for Th, U, Pu, and Cm isotopes, respectively. Theoretical values obtained using the present model are labeled as "Theor.", while experimental values are indicated as "Expt.". The experimental data is sourced from Refs.[12] and is measured in MeV. It is important to note that the typical uncertainty in the experimental values, estimated based on variations among different compilations, is approximately ± 0.5 MeV[12].

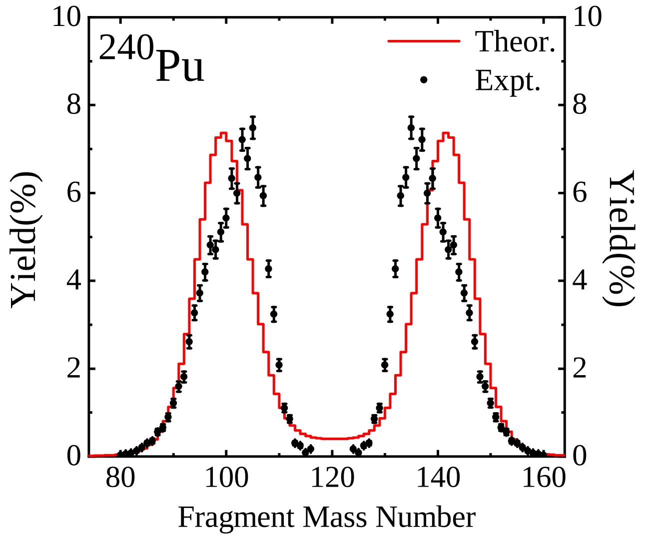

Fig. 4. (Color online) Mass yield of ^{240}Pu and compared with experimental data [72].

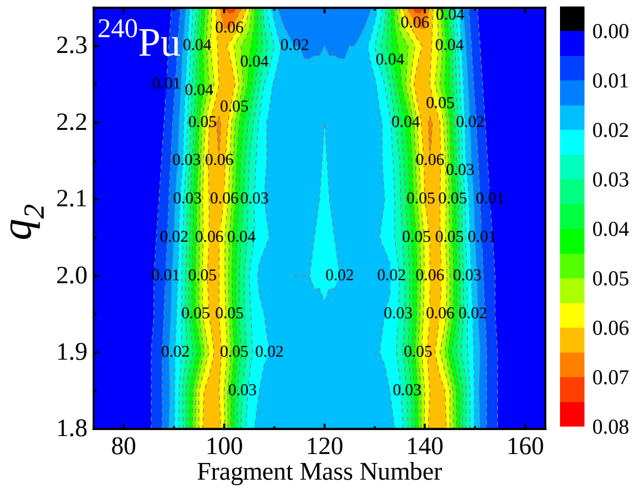

Fig. 5. (Color online) Mass yield of ^{240}Pu as a function of the mass number A_f and the elongation deformation q_2.

IV. EFFECT OF PAIRING INTERACTION ON THE FRAGMENT MASS DISTRIBUTIONS OF ^{230}Th, ^{234}U, ^{240}Pu, AND ^{246}Cm

The investigation of dynamics around fission structures plays a crucial role in comprehending various aspects of the final fission state, such as kinetic energy and mass distributions [7, 70, 71]. In this study, the fission fragment mass distribution of ^{240}Pu was calculated based on its potential energy surface and compared with experimental data [72].

As shown in Fig. 4, the agreement between the calculated results and experimental data is reasonable [72]. Moreover, the obtained fission fragment mass distribution aligns with the understanding that static fission in ^{240}Pu is predominantly asymmetric, as indicated by the fission potential energy surface. In the calculation process, a Gaussian folded function with a full width at half maximum (FWHM) of 4.9u [73] is employed to determine the mass yields. Additionally, two parameters, $E_0 = 2.2$ MeV and $d = 1.6$fm [49], are utilized.

In the case of fission nuclei, each elongation deformation variable q_2 corresponds to a distribution of fragment mass numbers A_f of the nuclear fragments produced during fission. Figure 5 illustrates the distribution of fragment mass numbers for ^{240}Pu. It is observed that fission predominantly occurs in the region of asymmetric fission, with the corresponding mass numbers of the heavy fragments centered around $A \approx 141$. The scission point, representing the point of fragment separation, is located at $q_2 = 2.3$. Only a small portion of fragments undergo symmetric fission.

To investigate the influence of the pairing interaction on the fission fragment mass distribution under the current model, we calculated the yield of the fission fragment as a function of mass numbers (A_f) for ^{230}Th, ^{234}U, ^{240}Pu, and ^{246}Cm with different pairing interaction strengths. The results depicted in Fig. 6 indicate that for these nuclei, as the pairing interaction strength G increases from $80\%G_0$ to $120\%G_0$, the two asymmetric peaks of the theoretical yield are significantly reduced, while the symmetric valley becomes more prominent. Similar observations were reported in a three-dimensional Langevin model based on the BCS approximation [74]. These findings suggest that the fragment mass distribution is sensitive to variations in the pairing interaction strength and highlight the significant role of pairing interaction in determining the fragment mass distribution for ^{230}Th, ^{234}U, ^{240}Pu, and ^{246}Cm. Furthermore, when the pairing interaction strength G is set to $120\%G_0$, the theoretical calculations closely match the experimental data for the fragment mass distribution of ^{230}Th, ^{234}U, and ^{240}Pu. However, for ^{246}Cm, the calculated results align better with the experimental values at a pairing interaction strength of $80\%G_0$.

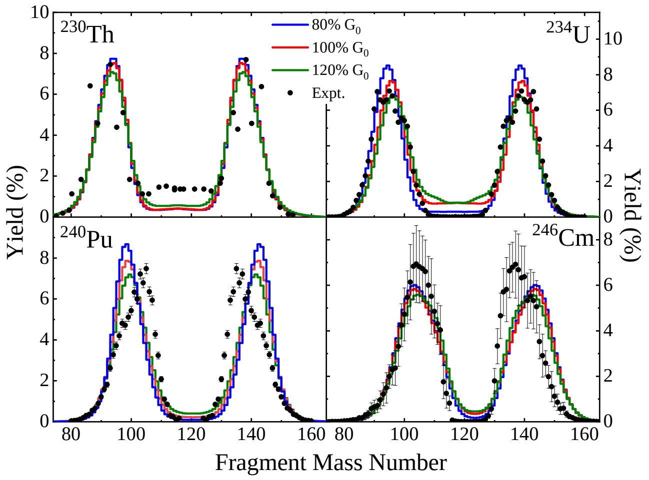

Fig. 6. (Color online) Mass yields for ^{230}Th, ^{234}U, ^{240}Pu, and ^{246}Cm as a function of mass numbers (A_f) with varying pairing interaction strengths. Experimental data for ^{230}Th are extracted from the charge-yields as reported in Ref [65]. The mass yields for ^{234}U are obtained from Ref [75]. For ^{240}Pu , the calculated mass yields are compared with experimental data [72]. The experimental data for ^{246}Cm are taken from Ref. [76].

Figure 7 illustrates the calculated odd-even mass differences at the asymmetric and symmetric fission points for ^{230}Th, ^{234}U, ^{240}Pu, and ^{246}Cm, considering the variation of the pairing strength G ranging from $80\%G_0$ to $120\%G_0$. In this analysis, it is assumed that the ground-state odd-even mass differences represent the odd-even binding-energy differences in the scission configuration, despite some shape differences. By comparing the experimental odd-even mass differences of asymmetric and symmetric fission fragments in nuclei such as ^{230}Th, ^{234}U, ^{240}Pu, and ^{246}Cm, the calculated results show better agreement with experimental values at the asymmetric fission point when the pairing strength is set to $120\%G_0$ for ^{230}Th, ^{234}U, and ^{240}Pu. Conversely, at the symmetric fission point, a stronger pairing interaction is required, and the calculated results agree better with experimental values when the pairing strength is set to $140\%G_0$ for ^{230}Th, ^{234}U, and ^{240}Pu. The calculated results for the odd-even mass differences at the symmetric and asymmetric fission points for ^{246}Cm demonstrate that pairing strengths of $80\%G_0$ and $120\%G_0$ match well with experimental values. This finding aligns with the earlier conclusion that increasing the pairing interaction strength leads to a better distribution of fission fragment masses for for ^{230}Th, ^{234}U, and ^{240}Pu.

The calculations presented above suggest that to achieve a better description of fission products, different elongation deformations of nuclei require different strengths of the pairing interaction. By fitting the ground-state binding energy, inner and outer barrier heights, and mass distribution calculations for Pu isotopes, the optimal values for the strength of

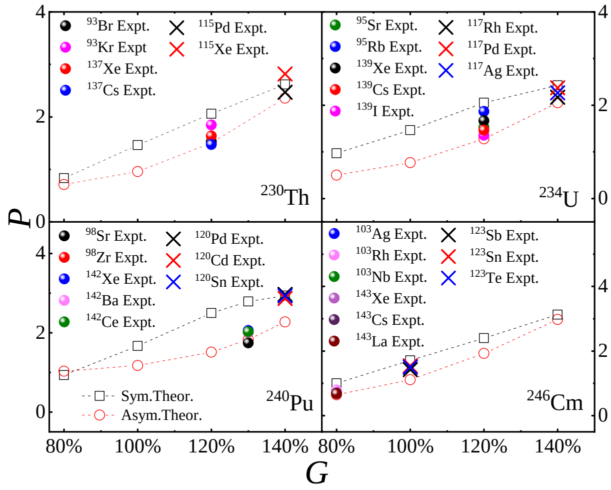

Fig. 7. (Color online) Odd-even mass differences (in MeV) of ^{230}Th, ^{234}U, ^{240}Pu, and ^{246}Cm at the asymmetric scission point and the symmetric scission point with varying pairing interaction strengths $G^{\nu(\pi)}$ from $80\%G_0$ to $120\%G_0$ (in MeV). The theoretical values calculated in the present model based on Eq. (26) in Ref. [60] are represented as "Sym.Theor." for symmetric point and "Asym.Theor." for asymmetric point. The experimental values of the odd-even mass difference for asymmetric and symmetric fission fragments of ^{230}Th, ^{234}U, ^{240}Pu, and ^{246}Cm denoted as "Expt." are obtained from Ref. [66] (in MeV).

the pairing interactions have been determined. As depicted in Fig. 8, the strength of the pairing interactions exhibits a nonlinear variation with increasing elongation deformation of the nucleus. In comparison to the barrier height, a stronger interaction is required to accurately describe the fragment mass distribution.

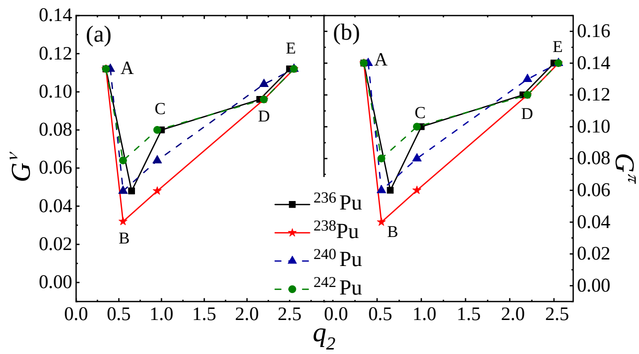

Fig. 8. (Color online) Pairing interaction strength G^{ν} (G^{π}) (in MeV) obtained by fitting the ground-state binding energy, inner and outer barrier heights, and fragment mass distribution calculations for $^{236-242}$Pu isotopes. Points (A)-(E) represent the corresponding q_2 values for the ground-state binding energy, inner and outer barrier heights, and the asymmetric and symmetric scission points.

V. FRAGMENT MASS DISTRIBUTION OF Th, U, Pu, AND Cm ISOTOPES

Based on the above results, this work calculates the fragment mass distribution of Th, U, Pu, and Cm isotopes chain based on the corresponding potential energy surface, with the pairing interaction strength set to $120\% G_0$. The theoretical calculations, as shown in Fig. 9, exhibit good agreement with experimental data for all isotopes. The peak height, peak width, and peak position of the fragment mass distribution closely match the experimental data. However, there are some discrepancies for specific isotopes, which can be attributed to the limitations of available experimental data.

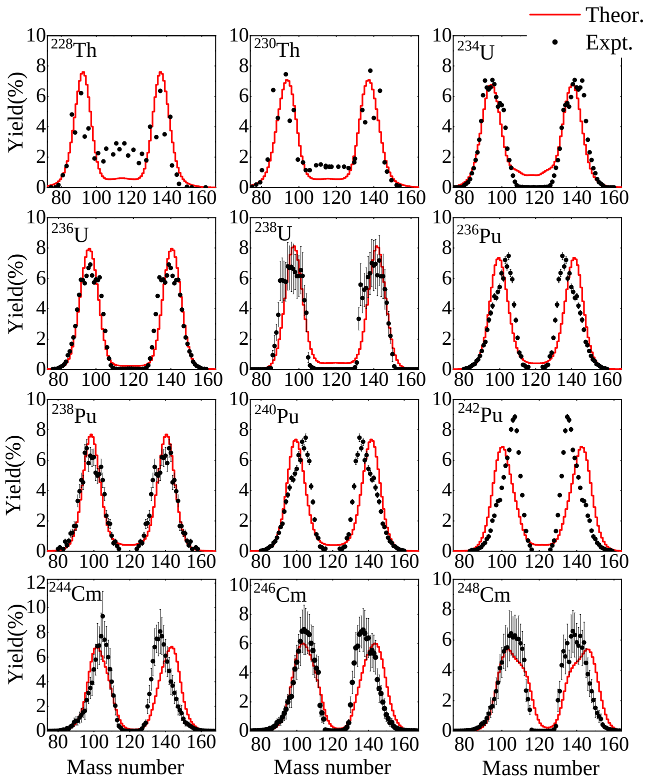

Fig. 9. (Color online) Mass yields for Th, U, Pu, and Cm isotopes as a function of mass numbers (A_f). Theoretical values calculated using the present model are represented as "Theor." while experimental data is denoted as "Expt." [75]. The experimental data for ^{228}Th and ^{230}Th are obtained by converting the charge distribution with an excitation energy of 11 MeV [65]. For the isotopes ^{234}U, ^{236}U, and ^{242}Pu, the experimental data used is from thermal neutron-induced fission [77], while for ^{236}Pu, ^{238}Pu, and ^{240}Pu, the data is from spontaneous fission experiments [76]. The evaluated post-neutron data for ^{238}U and $^{244-248}$Cm are taken from ENDF/B-VIII.0 [76].

For ^{228}Th and ^{230}Th, the experimental data for the fragment mass distribution were obtained by converting the charge distribution of the fragments at an excitation energy of 11 MeV in the fission system [65]. This may explain why the experimental value of the asymmetric mass yield of ^{228}Th is lower than the theoretical value, while the symmetric fission yield is relatively high. Experimental data from thermal neutron-induced fission were used for ^{234}U, ^{236}U [75]. The theoretical results show a higher symmetric valley for ^{234}U compared to the experimental data. For ^{238}U, due to a lack of available experimental data, evaluated post-neutron data from ENDF/B-VIII.0 were utilized [76].

Experimental data from spontaneous fission were used for ^{236}Pu, ^{238}Pu, and ^{240}Pu, and the calculated results closely match the experimental data in terms of peak width. For ^{242}Pu, experimental data from thermal neutron-induced fission were employed, and the calculated results exhibit similar peak width but deviate from the experimental data by $2-3$ mass units in peak position. For $^{244-248}$Cm isotopes, evaluated post-neutron data from ENDF/B-VIII.0 were used. The calculated results in Fig. 9 demonstrate good agreement with experimental data, indicating the effectiveness of the present model in reproducing the fission fragment mass distribution.

Overall, the model employed in this work successfully reproduces the experimental data of the fission fragment mass distribution for Th, U, Pu, and Cm isotopes, providing a valuable tool for understanding and analyzing fission processes.

VI. EFFECTS OF MODEL PARAMETERS ON FRAGMENT MASS DISTRIBUTION OF ^{240}Pu

In the subsequent research, the effects of the zero-point energy E_0 in Eq. (15) and the neck-breaking probability parameter d in Eq. (18) of the three-dimensional collective model on the fragment mass distribution of ^{240}Pu were investigated. The results, as depicted in Fig. 10-(a), indicate that the neck-breaking probability parameter d primarily influences the peak position of the asymmetric peak. When the neck-breaking probability parameter d increases, the peak position of the asymmetric peak shifts towards larger fragment masses.

On the other hand, the zero-point energy E_0 mainly affects the peak value of the fission fragments. As depicted in Fig. 10-(b), when the zero-point energy E_0 increases, the asymmetric peak value of the fission fragment mass distribution decreases. These observations are consistent with the findings reported in Reference [7]. These results highlight the importance of considering the zero-point energy and the neck-breaking probability parameter in the three-dimensional collective model for a more accurate description of the fragment mass distribution in fission processes.

VII. CONCLUSION

In summary, this article presents a comprehensive analysis of the fission process in Th, U, Pu, and Cm isotopes using a Yukawa-Folded mean-field plus standard pairing model. By employing a macroscopic-microscopic framework, the potential energy surfaces, fission paths, barriers, and fragment mass distributions were calculated. The study focused on investigating the impact of the pairing interaction on the mass distribution of fission fragments.

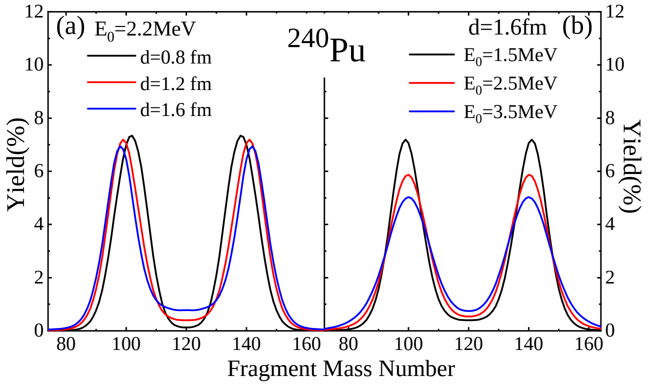

Fig. 10. (Color online) Mass yields of ^{240}Pu with different values of the zero-point energy E_0 in Eq. (15), and neck-breaking probability parameter d in Eq. (18).

Our results demonstrate that the pairing interaction plays a crucial role in shaping the fission process or ^{230}Th, ^{234}U, ^{240}Pu, and ^{246}Cm. The strength of the pairing interaction was determined by fitting experimental data of odd-even mass differences and barrier heights, which led to a better agreement between theory and experiment. Furthermore, we found that the fission fragment mass distribution is highly sensitive to changes in the pairing interaction strength for ^{230}Th, ^{234}U, ^{240}Pu, and ^{246}Cm, with stronger pairing interactions favoring symmetric fission and weaker interactions leading to more asymmetric fission. The odd-even mass differences for ^{230}Th, ^{234}U, ^{240}Pu, and ^{246}Cm at symmetric and asymmetric fission points were compared with experimental values, providing additional support for the findings regarding the role of the pairing interaction.

Moreover, by comparing our theoretical calculations with experimental data, we have confirmed the accuracy of our model in describing the fission fragment mass distributions for Th, U, Pu, and Cm isotopes. The peak heights, widths, and positions of the fragment mass distributions are well-reproduced, demonstrating the effectiveness of our approach.

Additionally, the study explores the effects of the zero-point energy parameter and neck-breaking probability parameter on the fragment mass distribution for ^{240}Pu. It is observed that the zero-point energy primarily influences the peak value of fission fragments, while the neck-breaking probability parameter affects the position of the asymmetric peak.

In conclusion, this research contributes to our understanding of the fission process by emphasizing the crucial role of the pairing interaction and its relationship with nuclear elongation. The well agreement between theoretical calculations and experimental data, along with the analysis of additional parameters, strengthens the validity and applicability of the proposed model. The insights gained from this study can inform future investigations in the field of nuclear fission, ultimately advancing our knowledge of this fundamental process.

[1] M. Bender, R. Bernard , G. Bertsch et al., Future of Nuclear Fission Theory. Journal of Physics G: Nuclear and Particle Physics **47**, (11) 113002 (2020). doi: 10.1088/1361-6471/abab4f

[2] A. Bulgac, Fission-fragment excitation energy sharing beyond scission. Phys. Rev. C **102**, 044609 (2020). doi: 10.1103/PhysRevC.102.044609

[3] A. Bulgac, P. Magierski, K. J. Roche et al., Nuclear Reactions and Superfluid Time Dependent Density Functional Theory. Phys. Rev. Lett. **116**, 122504 (2016). doi: 10.2174/9781681087641119020008

[4] J. Zhao, T. Nikšić, Dario Vretenar et al., Time-dependent generator coordinate method study of fission: Mass parameters. Phys. Rev. C **101**, 064605 (2020). doi: 10.1103/PhysRevC.101.064605

[5] J. C. Pei, W. Nazarewicz, J. A. Sheikh et al., Fission Barriers of Compound Superheavy Nuclei. Phys. Rev. Lett. **102**, 192501 (2009). doi: 10.1103/PhysRevLett.102.192501

[6] K. H. Schmidt and B. Jurado, Review on the progress in nuclear fission-experimental methods and theoretical descriptions. Rep. Prog. Phys. **81**, 106301 (2018). doi: 10.1088/1361-6633/aacfa7

[7] K. Pomorski, A. Dobrowolski , R. Han et al., Mass yields of fission fragments of Pt to Ra isotopes. Phys. Rev. C **101** 064602 (2020). doi: 10.1103/PhysRevC.101.064602

[8] M. R. Mumpower, P. Jaffke, M. Verriere et al., Primary fission fragment mass yields across the chart of nuclides. Phys. Rev. C **101**, 054607 (2020). doi: 10.1103/PhysRevC.101.054607

[9] H. J. Krappe and K. Pomorski, Theory of Nuclear Fission, Lecture Notes in Physics 838 (Springer-Verlag, Berlin, 2012).

[10] K. Rutz, M. Bender, P. Reinhard et al., Pairing gap and polarisation effects. Phys. Lett. B **468**, 1 (1999). doi: 10.1016/S0370-2693(99)01190-9

[11] N. Schunck, D. Duke, H. Carr et al., Description of induced nuclear fission with Skyrme energy functionals: Static potential energy surfaces and fission fragment properties. Phys. Rev. C **90**, 054305 (2014). doi: 10.1103/PhysRevC.90.054305

[12] M. Samyn, S. Goriely and J. M. Pearson, Further explorations of Skyrme-Hartree-Fock-Bogoliubov mass formulas. V. Extension to fission barriers. Phys. Rev. C **72**, 044316 (2005). doi: 10.1103/PhysRevC.72.044316

[13] H. Abusara, A. V. Afanasjev and P. Ring, Fission barriers in actinides in covariant density functional theory: The role of triaxiality. Phys. Rev. C **82**, 044303 (2010). doi: 10.1103/PhysRevC.82.044303

[14] S. Karatzikos, A. V. Afanasjev, G. A. Lalazissis et al., The fission barriers in Actinides and superheavy nuclei in covariant density functional theory. Phys. Lett. B **689**, 72 (2010). doi: 10.1016/j.physletb.2010.04.045

[15] J. Sadhukhan, J. Dobaczewski, W. Nazarewicz et al., Pairing-induced speedup of nuclear spontaneous fission. Phys. Rev. C **90**, 061304(R) (2014). doi: 10.1103/PhysRevC.90.061304

[16] Wu Tsung-shyh, Tseng Chin-yen, The influences of pairing force on the properties of actinide nuclei. Acta Phys.Sin. **21** (5): 915 (1965).doi: 10.7498/aps.21.915

[17] Zhu Yei zhung, Lee Tes ching, Lee Ming shou, The pairing effects of nuclei on the angular distribution of the fission fragments. Acta Phys. Sin. **22** (2): 136 (1966).doi:

10.7498/aps22.136
[18] Qu-Fei song, Long Zhu, Hui Guo et al., Verification of neutron-induced fission product yields evaluated by a tensor decompsition model in transport-burnup simulations. Nucl. Sci. Tech. **34**, 32 (2023).doi:10.1007/s41365-023-01176-5
[19] Long Zhou, Si-Min Wang,De-Qing Fang et al., Recent progress in two-proton radioactivity. Nucl. Sci. Tech. **33**, 105 (2022). doi:10.1007/s41365-022-01091-1
[20] Xing-Chen Ming, Hong-Fei Zhang, Rui-Rui Xu et al., Nuclear mass based on the multi-task learning neural network method. Nucl. Sci. Tech. **33**, 48 (2022). doi:10.1007/s41365-022-01031-z
[21] Yu-Feng Gao, Bo-Shuai Cai, Cen-Xi Yuan, Investigation of β^--decay half-life and delayed neutron emission with uncertainty analysis. Nucl. Sci. Tech. **34**, 9 (2023). https://doi.org/10.1007/s41365-022-01153-4
[22] H. Goutte, J. F. Berger, P. Casoli et al., Microscopic approach of fission dynamics applied to fragment kinetic energy and mass distributions in ^{238}U. Phys. Rev. C **71**, 024316 (2005). doi: 10.1103/PhysRevC.71.024316
[23] J. Sadhukhan, W. Nazarewicz and N. Schunck, Microscopic modeling of mass and charge distributions in the spontaneous fission of ^{240}Pu. Phys. Rev. C **93**, 011304(R) (2016). doi: 10.1103/PhysRevC.93.011304
[24] H. Tao, J. Zhao, Z. P. Li et al., Microscopic study of induced fission dynamics of ^{226}Th with covariant energy density functionals. Phys. Rev. C **96**, 024319 (2017). doi: 10.1103/PhysRevC.96.024319
[25] Z. Matheson, S. A. Giuliani, W. Nazarewicz et al., Cluster radioactivity of $^{294}_{118}\mathrm{Og}_{176}$. Phys. Rev. C **99**, 041304(R) (2019). doi: 10.1103/PhysRevC.99.041304
[26] Z. Łojewski and A. Staszczak, Role of pairing degrees of freedom and higher multipolarity deformations in spontaneous fission process. Nucl. Phys. A **657**, 134 (1999). doi: 10.1016/S0375-9474(99)00328-0
[27] M. Mirea and R. C. Bobulescu, Cranking mass parameters for fission. J. Phys. G **37**, 055106 (2010). doi: 10.1088/0954-3899/37/5/055106
[28] S. A. Giuliani, Z. Matheson, W. Nazarewicz et al., Colloquium: Superheavy elements: Oganesson and beyond. Rev. Mod. Phys. **91**, 011001 (2019). doi: 10.1103/RevModPhys.91.011001
[29] J. Zhao, B.-N. Lu, T. Nikšić et al., Multidimensionally-constrained relativistic mean-field study of spontaneous fission: Coupling between shape and pairing degrees of freedom. Phys. Rev. C **93**, 044315 (2016). doi: 10.1103/PhysRevC.93.044315
[30] J. Zhao, T. Nikšić and D. Vretenar, Microscopic self-consistent description of induced fission: Dynamical pairing degree of freedom. Phys. Rev. C **104**, 044612 (2021). doi: 10.1103/PhysRevC.104.044612
[31] Y. Qiang, J. C. Pei and P. D. Stevenson, Fission dynamics of compound nuclei: Pairing versus fluctuations. Phys. Rev. C **103**, L031304 (2021). doi: 10.1103/PHYSREVC.103.L031304
[32] X. Guan and C. Qi, An iterative approach for the exact solution of the pairing Hamiltonian. Comp. Phys. Comm. **275**, 108310 (2022). doi: 10.1016/j.cpc.2022.108310
[33] X. Y. Liu, C. Qi, X. Guan et al., PairDiagSph: Generalization of the exact pairing diagonalization program for spherical systems. Comp. Phys. Comm. **263**, 1107897 (2021). doi: 10.1016/j.cpc.2021.107897
[34] X. Guan, Y. Xin, Y. J. Chen et al., Impact of the pairing interaction on fission in the deformed mean-field puls standard pairing model. Phys. Rev. C **104**, 044329 (2021). doi: 10.1103/PhysRevC.104.044329
[35] X. Guan, T. C. Wang, W. Q. Jiang et al., Impact of the pairing interaction on fission of U isotopes. Phys. Rev. C **107**, 034307 (2023). doi: 10.1103/PhysRevC.107.034307
[36] R. W. Richardson, A restricted class of exact eigenstates of the pairing-force Hamiltonian. Phys. Lett. **3**, 277 (1963). doi: 10.1016/0031-9163(63)90259-2; Application to the exact theory of the pairing model to some even isotopes of lead. Phys. Lett. **5**, 82 (1963). doi: 10.1016/S0375-9601(63)80039-0;
[37] R. W. Richardson and N. Sherman, Pairing models of Pb^{206}, Pb^{204} and Pb^{202}. Nucl. Phys. **52**, 221 (1964); **52**, 253 (1964). doi: 10.1016/0029-5582(64)90690-X
[38] M. Gaudin, Diagonalization of a Class of Spin Hamiltonians. J. Physique **37**, 1087 (1976). doi: 10.1051/jphys:0197600370100108700
[39] F. Pan, J. P. Draayer and W. E. Ormand, A particle-number-conserving solution to the generalized pairing problem. Phys. Lett. B **422**, 1 (1998). doi: 10.1016/S0370-2693(98)00034-3
[40] J. Dukelsky, C. Esebbag and S. Pittel, Electrostatic Mapping of Nuclear Pairing. Phys. Rev. Lett. **88**, 062501 (2002). doi: 10.1103/PhysRevLett.88.062501
[41] J. Dukelsky, S. Pittel and G. Sierra, Colloquium: Exactly solvable Richardson-Gaudin models for many-body quantum systems. Rev. Mod. Phys. **76**, 643 (2004). doi: 10.1103/RevModPhys.76.643
[42] A. Faribault, O. El Araby, C. Sträter et al., Gaudin models solver based on the correspondence between Bethe ansatz and ordinary differential equations. Phys. Rev. B **83**, 235124 (2011). doi: 10.1103/PhysRevB.83.235124
[43] O. El Araby, V. Gritsev and A. Faribault, Bethe ansatz and ordinary differential equation correspondence for degenerate Gaudin models. Phys. Rev. B **85**, 115130 (2012). doi: 10.1103/PhysRevB.85.115130
[44] X. Guan, K. D. Launey, M. X. Xie et al., Numerical algorithm for the standard pairing problem based on the Heine-Stieltjes correspondence and the polynomial approach. Comp. Phys. Commun. **185**, 2714 (2014). doi: 10.1016/j.cpc.2014.05.023
[45] C. Qi and T. Chen, Exact solution of the pairing problem for spherical and deformed systems. Phys. Rev. C **92**, 051304(R) (2015). doi: 10.1103/PhysRevC.92.051304
[46] X. Guan, K. D. Launey, M. X. Xie et al., Heine-Stieltjes correspondence and the polynomial approach to the standard pairing problem. Phys. Rev. C **86**, 024313 (2012). doi: 10.1103/PhysRevC.86.024313
[47] C. Schmitt, K. Pomorski, B. K. Nerlo-Pomorska et al., Performance of the Fourier shape parametrization for the fission process. Phys.Rev.C **95**, 034612 (2017). doi: 10.1103/PhysRevC.95.034612
[48] L. L. Liu, Y. J. Chen, X. Z. Wu et al., Analysis of nuclear fission properties with the Langevin approach in Fourier shape parametrization. Phys.Rev. C **103**, 044601 (2021). doi: 10.1103/PhysRevC.103.044601
[49] K. Pomorski, J. M. Blanco, P. V. Kostryukov et al., Fission fragment mass yields of Th to Rf even-even nuclei. Chin. Phys. C **45** 054109 (2021). doi: 10.1088/1674-1137/abec69
[50] B. Nerlo-Pomorska, K. Pomorski and F. A. Ivanyuk, Fission fragments mass distribution of ^{236}U. Acta Phys. Pol. B Suppl. **8**, 659 (2015). doi: 10.5506/APhysPolBSupp.8.659
[51] K. Pomorski, F. A. Ivanyuk and B. Nerlo-Pomorska, Mass distribution of fission fragments within the Born-Oppenheimer approximation. Eur. Phys. J. A **53**, 59 (2017).

doi: 10.1140/epja/i2017-12250-5

[52] K. Pomorski, B. Nerlo-Pomorska, J. Bartel et al., Fission fragment mass and total kinetic energy distributions of spontaneously fissioning plutonium isotopes. Eur. Phys. J. Web Conf. 169, 00016 (2018). doi: 10.1051/epjconf/201816900016

[53] J. Randrup, S. E. Larsson, P. Möller et al., Spontaneous-fission half-lives for even nuclei with $Z \geq 92$. Phys. Rev. C **13**, 229 (1976). doi: 10.1103/PhysRevC.13.229

[54] K. Pomorski and J. Dudek, Nuclear liquid-drop model and surface-curvature effects. Phys. Rev. C **67**, 044316 (2003). doi: 10.1103/PhysRevC.67.044316

[55] P. Moller, J. R. Nix, W. D. Myers et al., Nuclear Ground-State Masses and Deformations. At. Data Nucl. Data Tables 59, 185 (1995). doi: 10.1006/adnd.1995.1002

[56] V. M. Strutinsky, Shell effects in nuclear masses and deformation energies. Nucl. Phys. A **95**, 420 (1967). doi: 10.1016/0375-9474(67)90510-6

[57] V. M. Strutinsky, Shells in deformed nuclei. Nucl. Phys. A **122**, 1 (1968). doi: 10.1016/0375-9474(68)90699-4

[58] R. Capote, M. Herman a b, P. Obložinský a b et al., RIPL-Reference Input Parameter Library for Calculation of Nuclear Reactions and Nuclear Data Evaluations. Nucl. Data Sheets **110**, 3107 (2009). doi: 10.1016/j.nds.2009.10.004

[59] Y. Sun, Projection techniques to approach the nuclear many-body problem. Phys. Scr. **91**, 043005 (2016). doi: 10.1088/0031-8949/91/4/043005

[60] M. Bender, K. Rutz, P.-G. Reinhard et al., Pairing gaps from nuclear mean-field models. Eur. Phys. J. A **8**, 59 (2000). doi: 10.1007/s10050-000-4504-z

[61] Y. Z. Wang, F. Z. Xing, J. P. Cui et al., Roles of tensor force and pairing correlation in two-proton radioactivity of halo nuclei. Chinese Physics C **47**, 084101 (2023). doi: 2023.10.1088/1674-1137/acd680

[62] Y. Z. Wang, Y. Li, C. Qi et al., Pairing Effects on Bubble Nuclei. Chinese Phys. Lett. **36**, 032101 (2019). doi: 10.1088/0256-307X/36/3/032101

[63] P. Möller, A. J. Sierk, T. Ichikawa et al., Heavy-element fission barriers. Phys. Rev. C **79**, 064304 (2009). doi: 10.1103/PhysRevC.79.064304

[64] I. V. Ryzhov, S. G. Yavshits, G. A. Tutin et al., Fragment-mass distributions in neutron-induced fission of $^{232}\mathrm{Th}$ and $^{238}\mathrm{U}$ at 33, 45, and 60. MeV. Phys. Rev. C, **83** 054603 (2011). doi: 10.1103/PhysRevC.83.054603

[65] K.H. Schmidt, S. Steinhuser, and C. Bckstiegel, Relativistic radioactive beams: A new access to nuclear-fission studies. Nucl. Phys. A, **665** 221 (2000). doi: 10.1016/S0375-9474(99)00384-X

[66] U.S. National Nuclear Data Center: http://www.nndc.bnl.gov/.

[67] P. Möller, A. J. Sierk, T. Ichikawa et al., Heavy-element fission barriers. Phys. Rev. C **79**, 064304 (2009). doi: 10.1103/PhysRevC.79.064304

[68] P. Jachimowicz, M. Kowal and J. Skalski, Static fission properties of actinide nuclei. Phys. Rev. C **101**, 014311 (2020). doi: 10.1103/PhysRevC.101.014311

[69] A. Dobrowolski, K. Pomorski and J. Bartel, Fission barriers in a macroscopic-microscopic model. Phys. Rev. C **75**, 024613 (2007). doi: 10.1103/PhysRevC.75.024613

[70] N. Schunck and L. M. Robledo, Microscopic Theory of Nuclear Fission: A Review. Rep. Prog. Phys,**79** 116301 (2016). doi: 10.1088/0034-4885/79/11/116301

[71] G. F. Bertsch, W. Younes and L. M. Robledo, Scission dynamics with K partitions. Phys. Rev. C **97** 064619, 2018. doi: 10.1103/PhysRevC.97.064619

[72] L.Demattè, C. Wagemans, R. Barthèlèmy et al., Fragments' mass and energy characteristics in the spontaneous fission of $^{236}\mathrm{Pu}$, $^{238}\mathrm{Pu}$, $^{240}\mathrm{Pu}$, $^{242}\mathrm{Pu}$, and $^{244}\mathrm{Pu}$. Nucl. Phys. A, **617**, 331 (1997). doi: 10.1016/S0375-9474(97)00032-8

[73] A. Göök, F.-J. Hambsch, S. Oberstedt et al., Prompt neutrons in correlation with fission fragments from $^{235}\mathrm{U(n,f)}$. Phys. Rev. C **98**, 044615 (2018). doi: 10.1103/PhysRevC.98.044615

[74] K. Pomorski and B. Nerlo-Pomorska, Acta Phys. Pol. B Proc. Suppl. **163**, 4-A21 (2023).

[75] P. Geltenbort and F. Goennenwein, A. Oed, Precision measurements of mean kinetic energy release in thermal-neutron-induced fission of $^{233}\mathrm{U}$, $^{235}\mathrm{U}$ and $^{239}\mathrm{Pu}$. Conf. on Nucl.Data f. Basic a. Appl.Sci., Santa Fe, 985, Vol. 1, p. 393 (1985). doi: 10.1080/00337578608207429

[76] K. H. Schmidt, B. Jurado, C. Amouroux et al., General Description of Fission Observables: GEF Model Code. Nucl. Data. Sheets,**131**, 107 (2016). doi: 10.1016/j.nds.2015.12.009

[77] P. Schillebeeckx, C. Wagemans, A. J. Deruytter et al., Comparative study of the fragments' mass and energy characteristics in the spontaneous fussion of $^{238}\mathrm{Pu}$, $^{240}\mathrm{Pu}$ and $^{242}\mathrm{Pu}$ and in the thermal-neutron-induced fission of $^{239}\mathrm{Pu}$. Nucl. Phys. A,**545**, 623 (1992). doi: 10.1016/0375-9474(92)90296-V